

# Nonlinear Hall effect induced by internal Coulomb interaction and phase relaxation process in a four-terminal system with time-reversal symmetry

Miaomiao Wei,<sup>1</sup> Bin Wang,<sup>1</sup> Yunjin Yu,<sup>1</sup> Fuming Xu,<sup>1,\*</sup> and Jian Wang<sup>1,2,†</sup>

<sup>1</sup>*College of Physics and Optoelectronic Engineering, Shenzhen University, Shenzhen 518060, China*

<sup>2</sup>*Department of Physics, University of Hong Kong, Pokfulam Road, Hong Kong, China*

We numerically investigate nonlinear Hall transport properties in a four-terminal system with time-reversal symmetry and broken inversion symmetry. Within the nonequilibrium Green's function formalism, the second-order nonlinear conductances are derived, where the internal Coulomb potential in response to external voltages is explicitly included to guarantee the gauge invariance. For the system with a single mirror symmetry  $\mathcal{M}_x$ , nonlinear Hall properties are only observable in the  $y$  direction and contributed solely from the second-order nonlinear effect. In addition to the intrinsic nonlinear Hall effect originated from nonzero Berry curvature dipole, it is found that the internal Coulomb potential has the same symmetry of the four-terminal system, which gives rise to an extra nonlinear Hall response. Furthermore, the phase relaxation mechanism modeled by virtual probes leads to additional dephasing-induced nonlinear Hall effect.

## I. INTRODUCTION

Conventional electric Hall effects in the linear response regime rely on the broken time-reversal symmetry, either by extrinsic magnetic fields or intrinsic magnetic materials. Counter-intuitively, in the nonlinear response regime, nonlinear Hall effect can exist in time-reversal-invariant materials without inversion symmetry, and its origin was attributed to the nonzero Berry curvature dipole in the band structure<sup>1-3</sup>. Several Weyl semimetal (WSM) materials<sup>4,5</sup> and two-dimensional transition metal dichalcogenides<sup>6,7</sup> were proposed as possible candidates to host Berry curvature dipole or the corresponding nonlinear Hall effect. It was soon confirmed by experiments in monolayer<sup>8</sup> and few-layer WTe<sub>2</sub><sup>9-11</sup>, as well as Weyl semimetal TaIrTe<sub>4</sub><sup>12</sup>, which are all time-reversal invariant and noncentrosymmetric materials. These experimental progresses have attracted intensive research interests on the Berry curvature dipole (BCD) and related topics<sup>13-24</sup>. For instance, either spin-orbit interactions<sup>7-10,13,14,17</sup> or warping of the Fermi surface<sup>18</sup> was found necessary to induce nonzero BCD in a time-reversal and inversion-broken system. Alternatively, the merging of a pair of Dirac nodes could also lead to finite BCD in 2-dimensional Dirac semimetals<sup>19</sup>. Except the nonlinear electric Hall current, BCD-caused nonlinear transport phenomena include nonlinear thermal effects driven by the temperature gradient<sup>25,26</sup> and nonlinear Hall photocurrent in Weyl semimetals<sup>5,20</sup>, etc.

While Berry curvature dipole is the band signature in momentum space, the resulting nonlinear Hall signals are detected on multi-terminal planar Hall bars in real space by experiments<sup>8-10,12</sup>. Therefore, it is necessary to study the nonlinear transport properties of four-terminal systems with nonzero Berry curvature dipole. Similar to the disorder effect, phase relaxation processes such as phonons and electron-electron interactions widely exist and have important influence in quantum transport. The virtual probe technique<sup>33</sup> is commonly used in modeling the phase relaxation process<sup>34-37</sup>. For example, it was both theoretically predicted<sup>27</sup> and experimentally verified<sup>28</sup> that, the electron dephasing due to virtual probes can lead to a positive cross correlation. In view of the disorder-induced nonlinear Hall effect<sup>29,30</sup>, it is interesting

to evaluate the influence of the dephasing mechanism on the four-terminal system with BCD, which is absent so far.

In this work, we study the nonlinear Hall effect, a manifestation of BCD, in a time-reversal-invariant four-terminal device with broken inversion symmetry. The second-order nonlinear Hall resistance and current as well as the transverse heat current are numerically investigated within the gauge invariant theory expressed in nonequilibrium Green's function. Since the internal Coulomb potential induced by electric response to external voltages is essential to guarantee the gauge invariance for nonlinear transport<sup>31,32</sup>, it is explicitly included in calculating the second-order nonlinear Hall properties. We find that the induced internal Coulomb potential has the same symmetry of the underlying system. Specifically, for the Hamiltonian with broken mirror symmetry  $\mathcal{M}_y$  in momentum space, the induced Coulomb potential is discovered to break  $\mathcal{M}_y$  in real space. As a result, an additional nonlinear Hall effect is generated due to this induced Coulomb potential. Because the induced Coulomb potential is always against the external electric field, this additional nonlinear Hall effect reduces the overall nonlinear Hall signal. The dephasing mechanism is also evaluated by employing the virtual probe. Similar to the internal Coulomb potential, the voltage profile of virtual probes has the same broken symmetry as the system, which introduces the dephasing-induced nonlinear Hall effect in addition to the intrinsic nonlinear Hall effect induced by BCD.

The rest of the paper is organized as follows. In section II, the gauge invariant theory is briefly reviewed and the second-order nonlinear conductance is defined. Section III starts with general analysis on relations between the linear and nonlinear conductances of a time-reversal-invariant four-terminal system with three typical spatial symmetries. Then the nonlinear Hall resistance and Hall current are numerically calculated along with detailed discussion. In addition, the dephasing effect and temperature influence are evaluated. A summary is finally given in section IV.

## II. GAUGE INVARIANT THEORY AND THE SECOND-ORDER NONLINEAR CONDUCTANCE

For a multi-terminal system, the current in terminal  $\alpha$  is calculated from the Landauer-Büttiker formula ( $\hbar = 1$ )<sup>38</sup>

$$I_\alpha = -q \sum_\beta \int_E Tr[\Gamma_\alpha G^r \Gamma_\beta G^a](f_\alpha - f_\beta), \quad (1)$$

where  $\int_E \equiv \int(dE/2\pi)$ ,  $\Gamma_\alpha = \Gamma_\alpha(E - qV_\alpha)$  is the linewidth function, and  $f_\alpha = f_\alpha(E - qV_\alpha)$  is the Fermi distribution function of terminal  $\alpha$ . The retarded Green's function  $G^r = G^r(E, U)$  depends on  $U$ , an internal self-consistent Coulomb potential that must be included into  $G^r$  to satisfy the gauge invariant condition.  $G^a = G^{r\dagger}$  is the advanced Green's function. In the Hartree approximation, the retarded Green's function in real space is given by

$$G^r(E, U) = \frac{1}{E - H - qU - \Sigma^r}, \quad (2)$$

where  $\Sigma^r = \sum_\alpha \Sigma_\alpha^r(E - qV_\alpha)$  is the self-energy which depends explicitly on external voltages, and  $\Gamma_\alpha = -2\text{Im}\Sigma_\alpha^r$ . The Coulomb potential  $U(x)$  satisfies the following self-consistent Poisson equation,

$$\nabla^2 U(x) = 4\pi i q \int_E [G^<(E, U)]_{xx}, \quad (3)$$

where  $x$  labels the position. The lesser Green's function  $G^<$  is given by  $G^< = G^r \Sigma^< G^a$  with

$$\Sigma^< = \sum_\beta i\Gamma_\beta(E - qV_\beta) f_\beta(E - qV_\beta). \quad (4)$$

Eq.(3) is, in general, a *nonlinear* equation since  $G^{r,a}$  depends on  $U(x)$ . Eqs.(1), (2), (3), and (4) form basic equations of the general gauge invariant DC transport theory. In quantum transport, one must calculate the Green's function along with the Poisson equation self-consistently. Clearly, the current expressed in Eq. (1) is gauge invariant: shifting the potential everywhere by a constant  $V$ ,  $U \rightarrow U + V$  and  $V_\alpha \rightarrow V_\alpha + V$ ,  $I_\alpha$  from Eq. (1) remains the same if we change the variable  $E$  to  $E - qV$ .

In the weakly nonlinear regime, we expand the Coulomb potential  $U(x)$  in the following form,

$$U(x) = U_{eq}(x) + \sum_\alpha u_\alpha(x) V_\alpha + \dots \quad (5)$$

where  $U_{eq}$  is the equilibrium potential when there is no external bias, and  $u_\alpha(x)$  is the characteristic potential<sup>31,39</sup> which describes the first-order internal response due to the Coulomb interaction to the external bias. As electrons are injected into the system, a nonequilibrium charge distribution is formed due to the long-range Coulomb interaction, which induces the internal Coulomb potential. This induced Coulomb potential maintains the gauge invariance for nonlinear quantum transport<sup>32</sup>, and closely related to the characteristic potential  $u_\alpha$ .

Expanding  $G^<$  from Eq. (3) in power of  $V_\alpha$ , we can derive the equations for all the characteristic potentials. Defining  $G_0^r = 1/(E - H - qU_{eq} - \Sigma_{eq}^r)$  and  $\Sigma_{eq}^r = \sum_\alpha \Sigma_\alpha^r(E)$  and using the Dyson equation, we have

$$G^r = G_0^r + G_0^r [qU - qU_{eq} + \Sigma^r - \Sigma_{eq}^r] G_0^r + \dots$$

with  $G_0^r$  the equilibrium retarded Green's function, *i.e.*, when  $U = U_{eq}$ . At the lowest order, we obtain from Eq.(3)<sup>31,40,41</sup>

$$-\nabla^2 u_\alpha = 4\pi q^2 \frac{dn_\alpha}{dE} - 4\pi q^2 \frac{dn}{dE} u_\alpha, \quad (6)$$

where  $dn_\alpha(x)/dE$  is the *injectivity* of terminal  $\alpha$ <sup>31,42,44</sup>,

$$\frac{dn_\alpha(x)}{dE} = - \int_E \partial_E f [G_0^r \Gamma_\alpha G_0^a]_{xx}, \quad (7)$$

and  $dn_\alpha(x)/dE$  satisfies the general relation<sup>31,32,40,45</sup>:

$$\sum_\alpha dn_\alpha(x)/dE = dn(x)/dE, \quad (8)$$

with  $dn(x)/dE$  the local charge density.

Clearly, the first term on the right-hand-side of Eq.(6) corresponds to the charge density due to external injection, while the second term describes the induced charge density in the system. Due to the gauge invariance, the characteristic potential  $u_\alpha$  follows the sum rule  $\sum_\alpha u_\alpha = 1$ <sup>31</sup>. The Thomas-Fermi approximation<sup>31</sup> is adopted in deriving Eq.(6).

The second-order nonlinear conductance  $G_{\alpha\beta\gamma}$  is defined by expanding the current in terms of external bias voltages to the second order<sup>40,46</sup>,

$$I_\alpha = \sum_\beta G_{\alpha\beta} V_\beta + \sum_{\beta\gamma} G_{\alpha\beta\gamma} V_\beta V_\gamma + \dots \quad (9)$$

with

$$G_{\alpha\beta\gamma} = G_{\alpha\beta\gamma}^e + G_{\alpha\beta\gamma}^i. \quad (10)$$

$G_{\alpha\beta\gamma}^e$  is the external contribution from injected free electrons,

$$G_{\alpha\beta\gamma}^e = -(q^3/2) \int_E \partial_E f \delta_{\beta\gamma} \text{Tr}[(\Gamma \delta_{\alpha\gamma} - \Gamma_\gamma) \times (G_0^a \Gamma_\alpha G_0^r G_0^r + G_0^a G_0^a \Gamma_\alpha G_0^r)], \quad (11)$$

while  $G_{\alpha\beta\gamma}^i$  is the internal contribution from the Coulomb potential,

$$G_{\alpha\beta\gamma}^i = q^3 \int_E \text{Tr}[(G_0^a \Gamma_\alpha G_0^r u_\beta G_0^r + G_0^a u_\beta G_0^a \Gamma_\alpha G_0^r) \times (\Gamma \delta_{\alpha\gamma} - \Gamma_\gamma)] \partial_E f, \quad (12)$$

where  $u_\beta$  is obtained from Eq.(6).

Finally, we symmetrize the definition of the second-order nonlinear conductance  $G_{\alpha\beta\gamma} := (1/2)(G_{\alpha\beta\gamma} + G_{\alpha\gamma\beta})$ . It is easy to see that the gauge invariance is equivalent to  $\sum_{\beta\gamma} G_{\alpha\beta\gamma} = 0$ <sup>47</sup>. The second-order nonlinear conductance of two-terminal systems has been numerically investigated using the scattering matrix approach<sup>48,49</sup>.

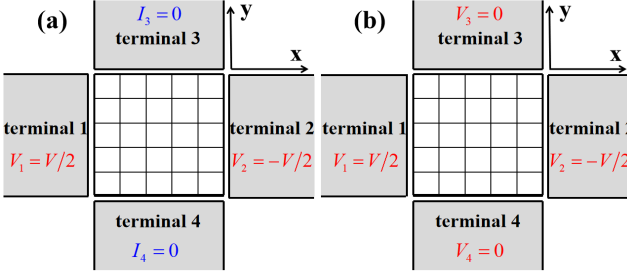


FIG. 1. (Color online) Schematic diagrams of the 2-dimensional four-terminal system with open (a) or closed (b) boundary condition.

### III. NUMERICAL RESULTS AND DISCUSSION

To study the Berry curvature dipole manifested in the nonlinear Hall effect, we choose the Hamiltonian with time-reversal (TR) symmetry and broken inversion symmetry<sup>50</sup>,

$$H(\mathbf{k}) = Ak^2 + (Bk^2 + \delta)\sigma_z + v_y k_y \sigma_y + D\sigma_x, \quad (13)$$

where  $A$ ,  $B$ , and  $D$  are system parameters, and  $\sigma_{x,y,z}$  are Pauli matrices. Such a low-energy Hamiltonian describes massive Dirac cones tilted by the  $v_y k_y \sigma_y$  term, which has been discussed in various Dirac systems<sup>1,29,51</sup>. To observe the nonlinear Hall effect, both nonzero  $D$  and  $v_y$  are required to break the inversion symmetry and generate a nonzero Berry curvature dipole. Note that this Hamiltonian breaks only the mirror symmetry  $\mathcal{M}_y$ :  $H(k_x, k_y) \neq H(k_x, -k_y)$  while preserves the mirror symmetry  $\mathcal{M}_x$ :  $H(k_x, k_y) = H(-k_x, k_y)$ . In the tight-binding presentation, this Hamiltonian is expressed in a square lattice as

$$H = \sum_{\mathbf{i}} \left[ \psi_{\mathbf{i}}^\dagger T_0 \psi_{\mathbf{i}} + \left( \psi_{\mathbf{i}}^\dagger T_x \psi_{\mathbf{i}+\mathbf{a}_x} + \psi_{\mathbf{i}}^\dagger T_y \psi_{\mathbf{i}+\mathbf{a}_y} \right) + H.c. \right],$$

where

$$\begin{aligned} T_0 &= -4T_x + \delta\sigma_z + D\sigma_x, \\ T_x &= -(AI + B\sigma_z)/a^2, \\ T_y &= T_x - iv_y \sigma_y / (2a). \end{aligned}$$

Here  $\psi_{\mathbf{i}}^\dagger$  is the creation operator at site  $\mathbf{i}$  with  $\mathbf{i} = (\mathbf{i}_x, \mathbf{i}_y)$  labeling the lattice site.  $\mathbf{a}_x = (a, 0)$  ( $\mathbf{a}_y = (0, a)$ ) is the unit vector in the  $x$  ( $y$ ) direction with  $a$  the lattice constant. In the calculation, we set  $A = 0$ ,  $B = 1$ ,  $\delta = -0.25$ ,  $v_y = 1.0$ ,  $D = 0.1$ , and  $a = 1$ .

As depicted in Fig. 1, two kinds of boundary conditions are considered to evaluate the linear and nonlinear Hall effects in typical four-terminal systems. In Fig. 1(a), bias voltages are applied in terminals 1 and 2 as  $V/2$  and  $-V/2$ , respectively. By setting  $I_3 = I_4 = 0$ , the transverse Hall voltage  $V_H$  across terminals 3 and 4 is measured:  $V_H = V_3 - V_4$ , and the corresponding Hall resistance  $R_H = V_H/I_1$  is obtained. We refer this setup as the open boundary condition<sup>52,53</sup>. In Fig. 1(b), when applying bias voltages in terminals 1 and 2 as  $V/2$  and  $-V/2$  and maintaining  $V_3 = V_4 = 0$ , the Hall current  $I_H = I_3 - I_4$  is probed. This case is referred as the

TABLE I. Relations of the linear conductances in the system with TR and different spatial symmetries.

System symmetry	Conductance symmetry
TR & inversion	$G_{11} = G_{22}, G_{33} = G_{44}, G_{13} = G_{14} = G_{23} = G_{24}$
TR & $M_x$ in real space	$G_{11} = G_{22}, G_{13} = G_{23}, G_{14} = G_{24}$
TR & $M_x$ in k-space	$G_{11} = G_{22}, G_{33} = G_{44}, G_{13} = G_{23} = G_{14} = G_{24}$

closed boundary condition. Similarly, one can also apply a bias across terminals 3 and 4 to measure the Hall resistance between terminals 1 and 2. As will be shown below, both the Hall resistance and Hall current reveal information of the Berry curvature dipole.

#### A. General discussion

In this subsection, we will derive and discuss relations among the linear and second-order nonlinear conductances defined in Eq.(9), when the time-reversal-invariant four-terminal system has different spatial symmetries. By engineering the Hamiltonian expressed in Eq.(13), three spatial symmetries: the inversion symmetry, the extrinsic mirror symmetry  $\mathcal{M}_x$  in real space, and the intrinsic mirror symmetry  $\mathcal{M}_x$  in momentum space, are presented in the following cases.

Case 1. The system with TR and inversion symmetries

We first study the case when both TR and inversion symmetries are preserved, which corresponds to that the linear term of  $k_y$  is dropped in Eq.(13). After the mirror symmetry  $\mathcal{M}_x$  transformation:  $H(k_x, k_y) \rightarrow H(-k_x, k_y)$ , external voltages change from  $(V_1, V_2, V_3, V_4)$  to  $(V_2, V_1, V_3, V_4)$  for the four-terminal system in Fig. 1. Subsequently, the currents vary from  $I_\alpha$  to  $I'_\alpha$  and follow these relations,

$$I_1 = I_2', I_2 = I_1', I_3 = I_3', I_4 = I_4', \quad (14)$$

$$I_1(V_1, V_2, V_3, V_4) = I_2(V_2, V_1, V_3, V_4). \quad (15)$$

Similarly, for the mirror symmetry  $\mathcal{M}_y$  transformation:  $H(k_x, k_y) \rightarrow H(k_x, -k_y)$ , bias voltages change from  $(V_1, V_2, V_3, V_4)$  to  $(V_1, V_2, V_4, V_3)$  in the device, and the currents satisfy

$$I_1 = I_1', I_2 = I_2', I_3 = I_4', I_4 = I_3', \quad (16)$$

$$I_3(V_1, V_2, V_3, V_4) = I_4(V_1, V_2, V_4, V_3). \quad (17)$$

For a system with inversion symmetry, its transport properties remain invariant under the change from  $(V_1, V_2, V_3, V_4)$  to  $(V_2, V_1, V_4, V_3)$ , so that the currents obey

$$I_1 = I_2', I_2 = I_1', I_3 = I_4', I_4 = I_3'. \quad (18)$$

From Eqs. (14)-(18) and  $G_{\alpha\beta\gamma} = G_{\alpha\gamma\beta}$ , relations among the linear conductances and second-order nonlinear conductances

TABLE II. Relations among the second-order nonlinear conductances in the system with both TR and inversion symmetries.

$G_{111} = G_{222}, G_{333} = G_{444}, G_{122} = G_{211}, G_{344} = G_{433}$
$G_{112} = G_{212}, G_{334} = G_{434}, G_{134} = G_{234}, G_{312} = G_{412}$
$G_{113} = G_{223} = G_{114} = G_{224}, G_{313} = G_{323} = G_{414} = G_{424}$
$G_{123} = G_{213} = G_{124} = G_{214}, G_{314} = G_{324} = G_{413} = G_{423}$
$G_{133} = G_{233} = G_{144} = G_{244}, G_{311} = G_{322} = G_{411} = G_{422}$

for the system with inversion symmetry are obtained and listed in the first row of Table I and Table II, respectively. Note that there are only seven independent coefficients in the second-order nonlinear conductance in this case.

Now we examine the nonlinear Hall effect up to the second order in voltage for the system with TR and inversion symmetries, where the Berry curvature is zero. To measure the Hall resistance, the open boundary condition is chosen as in Fig.1(a). Using Eqs.(17) and (9), it is easy to show that  $V_3 = V_4$  is the only physical solution, and hence both the linear and nonlinear Hall resistances are zero along the  $y$  direction. This is expected since zero Berry curvature leads to no Hall effect<sup>54</sup>. Similarly, there is neither no Hall effect along the  $x$  direction. If we apply bias voltages in terminals 3 and 4 as  $V/2$  and  $-V/2$ , and maintain zero bias in terminals 1 and 2, it is clear from Eq.(15) that  $I_1 = I_2$  indicating zero Hall current. Besides, one can always increase voltages of terminals 3 and 4 by a constant amount  $V_3 = V_4 = V_0$  to make  $I_1 = I_2 = 0$ , which leads to zero Hall voltage in the  $x$  direction. Therefore, for a four-terminal system with TR and inversion symmetries, both the linear and nonlinear Hall signals are zero.

Case 2. The system with TR and extrinsic mirror symmetry  $\mathcal{M}_x$  in real space

In this case, the linear term in  $k_y$  is removed in Eq.(13) and the mirror symmetry  $\mathcal{M}_y$  is preserved in momentum space. But  $\mathcal{M}_y$  is broken in real space by adding a potential with symmetry  $V(x, y) = V(-x, y)$ , and only the mirror symmetry  $\mathcal{M}_x$  is preserved in real space. From Eq. (14) and  $G_{\alpha\beta\gamma} = G_{\alpha\gamma\beta}$ , we show the relations for the linear and second-order nonlinear conductances in the second row of Table I and Table III, respectively. In this case, only Eq.(15) holds and hence there is no Hall effect along the  $x$  direction similar to the argument in Case 1. For the linear Hall effect along the  $y$  direction, we solve for  $V_3$  and  $V_4$  under the open boundary condition. From the second row of Table I and the Landauer-Büttiker formula, we have

$$\begin{aligned} I_3 &= G_{33}V_3 + G_{34}V_4 = 0, \\ I_4 &= G_{34}V_3 + G_{44}V_4 = 0, \end{aligned}$$

from which we find  $V_3 = V_4 = 0$  and the linear Hall resistance is zero. If we apply voltages in each terminal as  $\mathcal{V} = (V/2, -V/2, 0, 0)$ , i.e., the closed boundary condition, it is easy to show that  $I_3 = I_4 = 0$  and hence no linear Hall current as well. The nonlinear Hall response will be discussed

TABLE III. Relations between the second-order nonlinear conductances in the system with broken inversion symmetry.

$G_{111} = G_{222}, G_{122} = G_{211}, G_{311} = G_{322}, G_{411} = G_{422}$
$G_{112} = G_{212}, G_{134} = G_{234}, G_{313} = G_{323}, G_{413} = G_{423}$
$G_{133} = G_{233}, G_{144} = G_{244}, G_{114} = G_{224}, G_{314} = G_{324}$
$G_{124} = G_{214}, G_{414} = G_{424}, G_{113} = G_{223}, G_{123} = G_{213}$

in subsection B.

Case 3. The system with TR and intrinsic mirror symmetry  $\mathcal{M}_x$  in momentum space

In this case, the mirror symmetry  $\mathcal{M}_y$  is broken in momentum space while the spatial mirror symmetry  $\mathcal{M}_x$  is preserved in real space, which is exactly described by the tilted Hamiltonian Eq.(13). In such a situation, only the mirror symmetry  $\mathcal{M}_x$  is preserved in k-space, but the potential profile in real space has both mirror symmetries  $\mathcal{M}_x$  and  $\mathcal{M}_y$ . Consequently, the derivation leading to Eqs.(14) and (18) does not apply. It is because although the spatial inversion symmetry is preserved, electrons have different propagating velocities in  $x$  and  $y$  directions. The symmetry relations of  $G_{\alpha\beta\gamma}$  for this case are listed in the third row of Table I, which are derived in the Appendix and confirmed numerically.

For the second-order nonlinear conductance  $G_{\alpha\beta\gamma}$ , the induced Coulomb interaction has to be included to satisfy the gauge invariance. As will be shown in the next subsection, the induced Coulomb potential for the Hamiltonian Eq.(13) has mirror symmetry  $\mathcal{M}_x$  in real space while breaks the  $\mathcal{M}_y$  symmetry. Hence the relations among  $G_{\alpha\beta\gamma}$  are the same as those in Table III.

Now we discuss the procedure of calculating the nonlinear Hall resistance and current for the system governed by Eq.(13) with the second-order nonlinear theory derived in section II. Both open and closed boundary conditions are considered. When bias voltages are applied in terminals 1 and 2, the open boundary condition corresponds to  $I_3 = I_4 = 0$ , where  $I_3$  and  $I_4$  depend quadratically on the external bias as

$$I_3 = \sum_{\beta} G_{3\beta}V_{\beta} + \sum_{\beta\gamma} G_{3\beta\gamma}V_{\beta}V_{\gamma}, \quad (19)$$

$$I_4 = \sum_{\beta} G_{4\beta}V_{\beta} + \sum_{\beta\gamma} G_{4\beta\gamma}V_{\beta}V_{\gamma}. \quad (20)$$

Four solutions of  $V_3$  and  $V_4$  are obtained by solving two equations  $I_3 = I_4 = 0$ . Enforcing the following two constraints, only one physical solution is selected: (i) both  $V_3$  and  $V_4$  are real; (ii) the first-order current is much larger than the second-order one so that higher order terms can be neglected.

Recalling that  $G_{31} = G_{32}, G_{\alpha\beta\gamma} = G_{\alpha\gamma\beta}$  and  $V_1 = -V_2 = V/2$ , the quadratic equations  $I_3 = I_4 = 0$  is sim-

plified as

$$\begin{aligned} I_3 &= G_{33}V_3 + G_{34}V_4 + (G_{311} + G_{322} - 2G_{312})V_1^2 \\ &\quad + G_{333}V_3^2 + 2G_{334}V_3V_4 + G_{344}V_4^2 = 0, \\ I_4 &= G_{43}V_3 + G_{44}V_4 + (G_{411} - 2G_{412} + G_{422})V_1^2 \\ &\quad + G_{433}V_3^2 + 2G_{434}V_3V_4 + G_{444}V_4^2 = 0. \end{aligned} \quad (21)$$

If we restore the  $\mathcal{M}_y$  symmetry, the inversion symmetry is recovered and the Berry curvature vanishes. As a result, the physical solution is  $V_3 = V_4$ . However, for the system with broken  $\mathcal{M}_y$  symmetry, the physical solution  $V_3$  is not equal to  $V_4$ . Subsequently, the Hall voltage  $V_H = V_3 - V_4 \neq 0$  and the Hall resistance  $R_H = V_H/I_1 \neq 0$ .

As for the closed boundary condition, currents  $I_3$  and  $I_4$  are directly calculated from Eqs.(19) and (20). Apparently, the linear terms vanish,  $I_3^{1st} = \sum_{\beta} G_{3\beta}V_{\beta} = 0$ ,  $I_4^{1st} = \sum_{\beta} G_{4\beta}V_{\beta} = 0$ , given that  $G_{31} = G_{32}$ ,  $V_1 = -V_2 = V/2$ , and  $V_3 = V_4 = 0$ . However, the second-order currents are nonzero:

$$\begin{aligned} I_3 &= (G_{311} - G_{312})V^2/2, \\ I_4 &= (G_{411} - G_{412})V^2/2. \end{aligned} \quad (22)$$

It is clear from Table III that the second-order current  $I_3$  is not equal to  $I_4$  in a system with broken inversion symmetry, and hence the Hall current  $I_H = I_3 - I_4 \neq 0$ . When the applied bias is along the  $y$  direction, both the Hall resistance  $R_H$  and current  $I_H$  are zero in the  $x$  direction for the system with mirror symmetry  $\mathcal{M}_x$  due to Eq.(15), as discussed in previous cases. In summary, for an inversion-broken system with only the  $\mathcal{M}_x$  symmetry described by Eq.(13), nonlinear Hall effect only exists in the  $y$  direction and is contributed solely by the second-order nonlinear properties.

Our theoretical analysis is completely in agreement with the Boltzmann approach<sup>1</sup> at zero frequency. It was argued that<sup>1</sup>, for a 2-dimensional(2D) TR system with a single mirror symmetry, the Berry curvature dipole behaves like a *pseudovector* in the 2D plane and is forced to be perpendicular to the mirror line. When the driving electric field is aligned with the BCD vector, the flowing currents orthogonal to this driving field are solely contributed by the BCD term and leads to the nonlinear Hall effect<sup>1</sup>. In vector notation, this Hall current is proportional to  $\vec{D} \cdot \vec{E}$ , with  $\vec{D}$  the BCD vector and  $\vec{E}$  the electric field<sup>1</sup>. Therefore, if the applied electric field is perpendicular to the BCD vector,  $\vec{D} \cdot \vec{E} = 0$  and nonlinear Hall effects vanish. In our situation, for a system determined by Eq.(13), only the mirror symmetry  $\mathcal{M}_x$  is preserved and the mirror line is  $x = 0$ , i.e., the  $y$  axis. The resulting BCD vector has to be along the  $x$  axis. When bias voltages are applied across terminals 1 and 2 that is parallel to the BCD vector, nonlinear Hall properties from the second-order contributions are observed in the  $y$  direction. On the contrary, the Hall effect is absent when applying external voltages in terminals 3 and 4, since the driving electric field is perpendicular to the BCD vector. The consistency between our results and the previous study<sup>1</sup> confirms that the second-order nonlinear theory based on the nonequilibrium Green's function is appropriate in studying the BCD-induced nonlinear Hall effect.

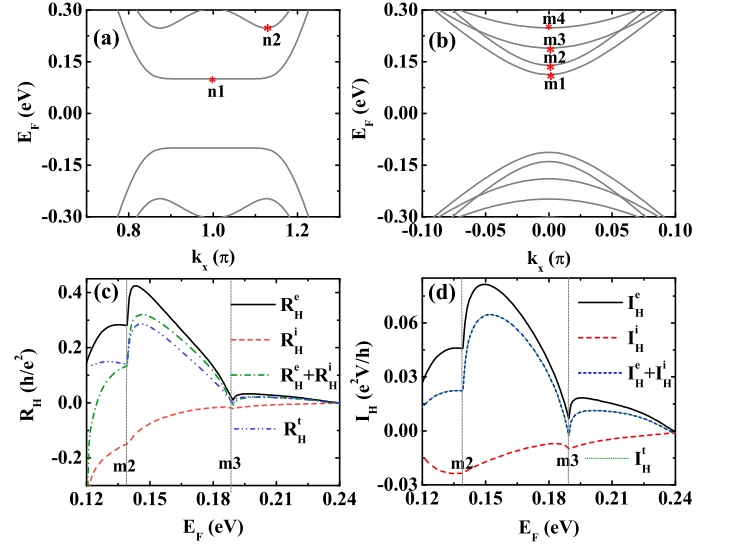


FIG. 2. (Color online) (a) and (b): Band structures of the system along  $x$  and  $y$  directions. The Hall resistance  $R_H$  (c) and Hall current  $I_H$  (d) versus the Fermi energy  $E_F$  in the four-terminal system.

## B. Numerical results on nonlinear Hall effect

In this subsection, we numerically investigate the nonlinear Hall properties of the inversion-broken system described in Eq.(13) on a square lattice. In the calculation, the size of the central region for the four-terminal system shown in Fig.1 is fixed as  $N = L \times L$  with  $L = 20$ . As a start, band structures of the system along  $x$  and  $y$  directions are plotted in Figs.2(a) and 2(b). Since the band structures are symmetric about  $E_F = 0$ , we only study the case of  $E_F > 0$ . To distinguish different subbands, the band edges are labeled with  $n_{\mathbf{j}}$  and  $m_{\mathbf{j}}$  for  $\mathbf{j} = 1, 2, \dots$ , respectively.

To study the role played by the internal Coulomb potential, we calculate  $G_{\alpha\beta\gamma}^e$  and  $G_{\alpha\beta\gamma}^i$  in Eq.(10) separately, to give the partial Hall resistances  $R_H^e$  and  $R_H^i$ , and similarly for the partial Hall currents  $I_H^e$  and  $I_H^i$ . For the total Hall current  $I_H^t$  calculated from Eq.(22) under the closed boundary condition, it is obvious that  $I_H^t$  is linearly proportional to  $G_{\alpha\beta\gamma}$ , and  $G_{\alpha\beta\gamma} = G_{\alpha\beta\gamma}^e + G_{\alpha\beta\gamma}^i$  leads to  $I_H^t = I_H^e + I_H^i$ . The situation is different for the total Hall resistance  $R_H^t$ . Since the Hall voltage  $V_H = V_3 - V_4$  is obtained by solving nonlinear equations in Eq.(21), the sum of  $R_H^e + R_H^i$  is not equal to  $R_H^t$ .

In calculating  $G_{\alpha\beta\gamma}^i$ , which is contributed by the internal Coulomb potential, the characteristic potential  $u_{\alpha}$  has to be solved. To avoid solving the Poisson equation self-consistently, we use the quasi-neutrality approximation<sup>31</sup> so that the local charge density is zero, from which the characteristic potential is found to be<sup>31,49</sup>,

$$u_{\alpha} = \frac{dn_{\alpha}}{dE} / \frac{dn}{dE}.$$

Since the nonlinear Hall current is directly proportional to the BCD vector<sup>1</sup>, both the nonlinear  $I_H$  and  $R_H$  reveal information of BCD from the inversion-broken system. In Figs.

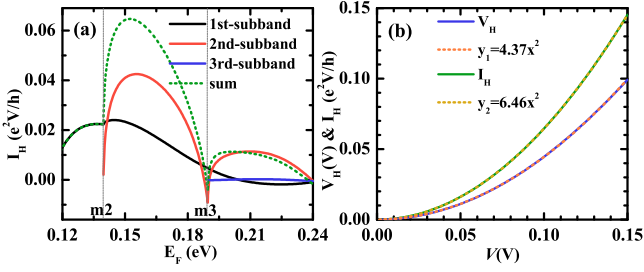


FIG. 3. (Color online) (a) Different subband contributions to the Hall current  $I_H$  versus the Fermi energy  $E_F$ . (b) The Hall voltage  $V_H$  (at  $E_F = 0.145$ ) and Hall current  $I_H$  (at  $E_F = 0.153$ ) versus the applied bias  $V$  along the  $x$  direction.

2(c) and 2(d), the Hall resistance and current versus the Fermi energy  $E_F$  are presented. The sum of  $R_H^c + R_H^i$  and  $I_H^e + I_H^i$  are also plotted for comparison. Several observations are in order. (1). The contribution from the Coulomb interaction is significant and has an opposite sign. It is understandable since the induced Coulomb potential is always against the external bias. (2). For the energy window shown in Fig.2, the injected electron traversing along the  $x$  direction is in the first transmission channel (Fig.2(a)), while the outgoing electron along the  $y$  direction can have several conducting channels ( $m1$ ,  $m2$  and  $m3$  in Fig.2(b)) due to the broken  $\mathcal{M}_y$  symmetry in momentum space. As the Fermi energy increases, the abrupt change in the Hall resistance or current originates from this subband nature. Moreover, at the third subband threshold  $m3$ , the total Hall current  $I_H^t$  is negative. If the  $I_H^i$  term contributed from the Coulomb potential is not included, the nonlinear Hall current would remain positive. Hence the induced Coulomb potential leads to a negative  $I_H^i$ . (3). The curves of  $R_H^t$  and  $I_H^t$  in Fig.2(c) and 2(d) have similar behaviors.  $I_H^t$  increases monotonically in the first subband. As the Fermi energy across the second subband threshold, one more transmission channel is open, giving rise to a jump in the Hall current. Entering the second subband,  $I_H^t$  continues to rise, reaches the maximum and then decreases monotonically until  $E_F$  hits the third subband. As shown in Fig.3(a) that the second subband contribution to  $I_H$  is positive. In the third subband, contributions from three transmission channels give a negative Hall current at the third subband threshold (see Fig.3(a)). As the Fermi energy increases, the first subband contribution to  $I_H$  becomes negative while the third subband contribution is two orders of magnitude smaller than that of the first and second subband. Overall, the Hall current behaves similarly as in the second subband. (4). With further increase of  $E_F$ , the energy bands are getting closer, and the difference between voltages  $V_3$  and  $V_4$  (the second-order currents  $I_3^{2nd}$  and  $I_4^{2nd}$ ) caused by the broken mirror symmetry  $\mathcal{M}_y$  is smaller. As a result, the nonlinear Hall voltage  $V_H$  and current  $I_H$  approach to zero when the Fermi energy  $E_F$  is far away from the gap.

The nonlinear characteristics of the Hall properties are shown in Fig.3(b), where  $V_H$  and  $I_H$  versus the applied bias voltage along the  $x$  direction are plotted.  $I_H$  in Fig.3(b) follows from Eq.(22) and increases quadratically with  $V$ .  $V_H$  in Fig.3(b) is approximately parabolic when  $V_1 = V/2$  is small.

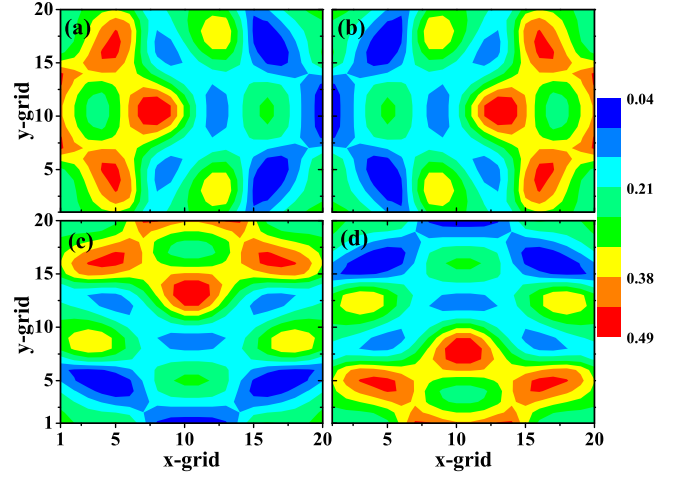


FIG. 4. (Color online) The characteristic potential  $u_1$  (a),  $u_2$  (b),  $u_3$  (c) and  $u_4$  (d) when both TR and inversion symmetry are present.

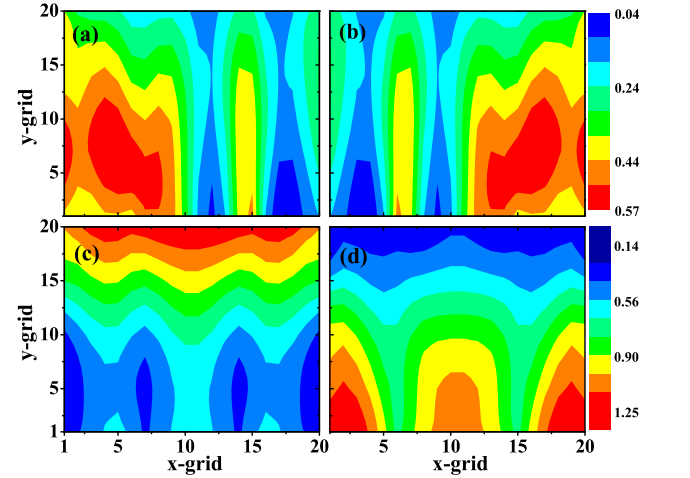


FIG. 5. (Color online) The characteristic potentials  $u_1$  (a),  $u_2$  (b),  $u_3$  (c) and  $u_4$  (d) for the TR system with mirror symmetry  $\mathcal{M}_x$ .

This is because when  $V_1$  is small,  $V_3$  and  $V_4$  are of order  $V_1^2$ . Therefore one can safely drop quadratic terms of  $V_3$  and  $V_4$  in Eq.(21) and immediately obtain  $V_3$  and  $V_4$  by solving linear equations.

To investigate the symmetry of the induced Coulomb potential, we plot in Fig.4 the characteristic potential  $u_\alpha$  ( $\alpha = 1, 2, 3, 4$ ) for Case 1 with both TR and inversion symmetries. The characteristic potential  $u_\alpha$  is related to the induced nonequilibrium Coulomb potential  $U_{neq}$  through  $U_{neq} = \sum_\alpha u_\alpha V_\alpha$  up to the first order in voltage (Eq.(5)). Note that  $u_\alpha$  originates from the injection from terminal  $\alpha$ . As a result, the potential profile of  $u_\alpha$  is always higher at the corresponding terminal  $\alpha$ . From Fig.4 we see that  $u_1(u_2)$  itself has the up-down symmetry, since electrons injected from the left or right terminal experience the mirror symmetry  $\mathcal{M}_y$  of the system. Clearly, the summation  $u_1 V_1 + u_2 V_2 = (u_1 - u_2)V/2$  has both  $\mathcal{M}_x$  and  $\mathcal{M}_y$  symmetries, which in fact is the inversion symmetry. Similar observations can be obtained through

analyzing the symmetry of  $u_3$ ,  $u_4$ , and  $u_3V_3 + u_4V_4$ .

As a result, the induced Coulomb potential, which is the summation of all  $u_\alpha V_\alpha$ , has the inversion symmetry. These facts indicate that the induced Coulomb potential preserves the same symmetry as that of the underlying system. Indeed, this statement is also valid for Case 3, i.e., the system with a single symmetry  $\mathcal{M}_x$ . Fig. 5 depicts the characteristic potential  $u_\alpha$  for Case 3. It is clear from  $u_3$  and  $u_4$  that electrons coming from the up or down terminal experience the mirror symmetry  $\mathcal{M}_x$ . However,  $u_1$  and  $u_2$  indicate that no spatial symmetry is undergone by electrons injected from the left or right terminal, and  $u_1V_1 + u_2V_2$  only recovers the  $\mathcal{M}_x$  symmetry. Hence, when the mirror symmetry  $\mathcal{M}_y$  is broken in k-space, the induced Coulomb potential has the broken mirror symmetry  $\mathcal{M}_y$  in real space. This nonequilibrium Coulomb potential in turn gives rise to an extra nonlinear Hall effect (NHE), in addition to the intrinsic nonlinear Hall effect caused by nonzero BCD of the inversion-broken system. The competition between the Coulomb potential induced NHE and the intrinsic NHE reduce the overall nonlinear Hall response, since the internal Coulomb potential is always against the bias and its contribution to  $R_H$  and  $I_H$  has opposite sign (Fig. 2).

### C. Nonlinear Hall effect in the presence of dephasing

Next, we study the nonlinear Hall effect in the presence of dephasing. The virtual probe method is used to simulate the dephasing process<sup>33</sup>. The virtual probe acts as a voltage probe that allows exchange of electrons between the scattering region and the reservoir but forbids the current passing through. The thermalization of electron entering virtual probe by dissipation makes the electron losing its phase memory. Here we show that dephasing can also cause an additional nonlinear Hall effect. In the calculation, we assume that the phase relaxation occurs only in the central region. A voltage probe is attached to each site  $\mathbf{i}$  with the constraint  $I_{\mathbf{i}} = 0$  so that dephasing is taken into account from the response of this virtual probe<sup>37</sup>. The Hamiltonian with virtual probes in momentum space is written as

$$H_{virtual} = \sum_{\mathbf{i},k} \varepsilon_k \psi_{\mathbf{i}k}^\dagger \psi_{\mathbf{i}k} + \sum_{\mathbf{i},k} \left( t_k \psi_{\mathbf{i}k}^\dagger \psi_{\mathbf{i}} + \text{H.c.} \right),$$

where  $\psi_{\mathbf{i}k}^\dagger$  ( $\psi_{\mathbf{i}k}$ ) is the creation (annihilation) operator of the electron in the virtual probe,  $t_k$  denotes the coupling strength between the virtual probe and the central region. In addition, the retarded self-energy of the virtual probe is  $\Sigma_{\mathbf{i}}^r = -i\Gamma/2$  with  $\Gamma$  the dephasing strength. The number of virtual probes equals to the size of the central region  $N = L \times L$ . Thus, including four real probes, there are total of  $N + 4$  probes. In the presence of dephasing, we still use open and closed boundary conditions to calculate the Hall resistance and current, respectively. Under the open boundary condition, with  $I_3 = I_4 = 0$ ,  $V_1 = -V_2 = V/2$  and  $N$  extra boundary conditions  $I_{\mathbf{i}} = 0$ , we can obtain the voltage profile of virtual probes, i.e., the bias  $v_{\mathbf{i}}$  at each virtual probe. Taking the contribution of virtual probes into account, the voltages  $V_3$  and  $V_4$  are obtained

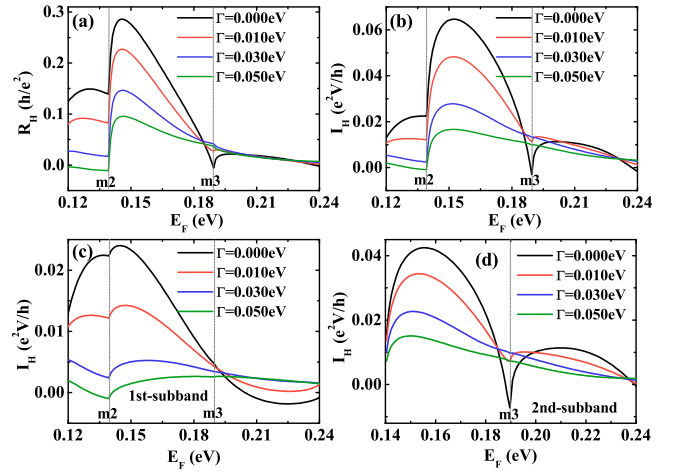


FIG. 6. (Color online) The Hall resistance  $R_H$  (a) and Hall current  $I_H$  (b) versus the Fermi energy  $E_F$  under different dephasing strengths. (c) and (d) show subband contributions to the Hall current.

by solving the quadratic equations

$$I_3 = \sum_{\beta} G_{3\beta} V_{\beta} + \sum_{\beta\gamma} G_{3\beta\gamma} V_{\beta} V_{\gamma} + \sum_{i=1}^N G_{3i} v_i = 0, \quad (23)$$

$$I_4 = \sum_{\beta} G_{4\beta} V_{\beta} + \sum_{\beta\gamma} G_{4\beta\gamma} V_{\beta} V_{\gamma} + \sum_{i=1}^N G_{4i} v_i = 0,$$

where the conductance from site  $\mathbf{i}$  to terminal  $\alpha$  is given by

$$G_{\alpha i} = \frac{e^2}{2\pi} \text{Tr} [\Gamma_{\alpha} G^r \Gamma_i G^a].$$

In this way, the Hall resistance  $R_H = (V_3 - V_4)/I_1$  can be obtained in the presence of dephasing. For the closed boundary condition, we solve for  $v_i$  at each virtual probe with  $V_3 = V_4 = 0$ ,  $V_1 = -V_2 = V/2$  and  $N$  extra boundary conditions  $I_{\mathbf{i}} = 0$ . Once  $v_i$  is calculated, the current  $I_3$  and  $I_4$  are expressed as

$$I_3 = \sum_{\beta} G_{3\beta} V_{\beta} + \sum_{\beta\gamma} G_{3\beta\gamma} V_{\beta} V_{\gamma} + \sum_{i=1}^N G_{3i} v_i,$$

$$I_4 = \sum_{\beta} G_{4\beta} V_{\beta} + \sum_{\beta\gamma} G_{4\beta\gamma} V_{\beta} V_{\gamma} + \sum_{i=1}^N G_{4i} v_i,$$

from which the Hall current  $I_H = I_3 - I_4$  is obtained under dephasing.

Numerical results of the dephasing effect on the nonlinear Hall properties are presented in Figs. 6(a) and 6(b). It is known that the dephasing effect can destroy the quantum interference<sup>33,55</sup>. Since the typical quantum interference phenomenon is exhibited in the resonance (resonant peak) and anti-resonance (resonant dip), we expect the phase relaxation process suppresses (enhances) the Hall resistance and current

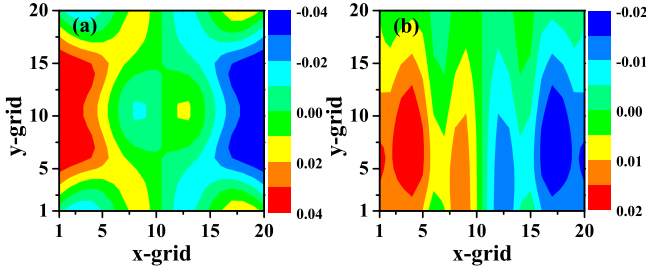


FIG. 7. (Color online) Voltage profile of virtual probes for the TR system with inversion symmetry (a) or mirror symmetry  $\mathcal{M}_x$  (b).

in the resonant region (off-resonant region)<sup>36</sup>. Different subband contributions to  $I_H$  are depicted in Fig.6(c) and (d). From Fig.6 we see that the Hall resistance and current decrease as a function of the Fermi energy in the first and second subbands as the dephasing strength increases. For a large enough dephasing strength,  $R_H$  and  $I_H$  can change sign at the closing of the first subband. Near the second subband, the dip in  $R_H$  and  $I_H$  are smeared out suggesting the anti-resonance nature of this dip. Furthermore, a moderate strength of dephasing leads to a sign change of  $I_H$  at the third subband threshold.

Finally, we show in Fig.7 the voltage profile of virtual probes for Case 1 and 3. Similar to the induced Coulomb potential, the voltage profile also has the same symmetry of the system. Another equivalent description of dephasing is to introduce a complex potential to mimic the inelastic scattering<sup>55</sup> or simulate the virtual probe setup. We realize that it is difficult to map the voltage profile to the complex potential. However, in view of the calculated voltage profile of virtual probes, this equivalent complex potential should have the mirror symmetry  $\mathcal{M}_x$  in real space, which is consistent with the fact that the nonlinear Hall effect is nonzero only along the  $y$  direction in the presence of dephasing. Therefore, from this perspective, the complex potential due to dephasing can lead to a dephasing-induced nonlinear Hall effect on top of the BCD-induced intrinsic NHE.

#### D. Nonlinear Hall effect at finite temperature

In this subsection, we study the nonlinear Hall resistance and Hall current at finite temperature. In Figs. 8(a) and 8(b), we plot  $R_H$  and  $I_H$  versus  $E_F$  for different temperatures. At finite temperatures, the thermal broadening effect smears out any resonance and anti-resonance. Generally speaking, the Hall resistance and current in the first subband increase with the rising of the temperature while in the second subband they decrease as seen from Fig.8. Around the third subband threshold  $R_H$  and  $I_H$  increase with temperature. In addition, the discontinuities at the second and third subband threshold are also smoothed out. Similar to the dephasing effect, as the temperature is turned on, the negative  $I_H$  at the third subband threshold becomes positive.

Since a moving electron also carries energy, the heat current

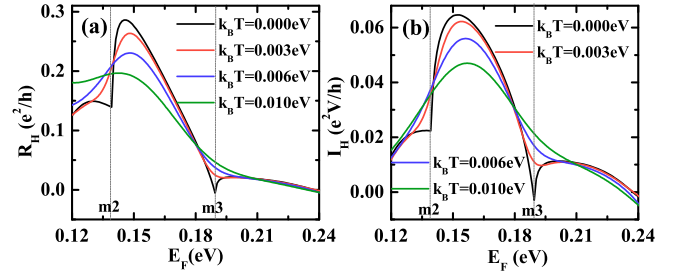


FIG. 8. (Color online) The Hall resistance  $R_H$ (a) and Hall current  $I_H$  (b) versus the Fermi energy  $E_F$  for different temperatures.

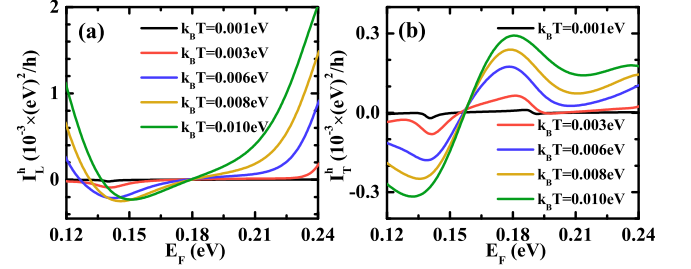


FIG. 9. (Color online) The longitudinal Heat current  $I_L^h$ (a) and transverse heat current  $I_T^h$ (b) versus the Fermi energy for different temperatures.

$I_\alpha^h$  is also calculated at finite temperatures. The heat current is defined as the sum of the momentum dependent particle current multiplied by its energy measured from the Fermi level<sup>56</sup>,

$$I_\alpha^h = q \int_E (E - E_F - qV_\alpha) \sum_\beta (f_\alpha - f_\beta) T_{\alpha\beta}, \quad (24)$$

where  $T_{\alpha\beta} = \text{Tr}[\Gamma_\alpha G^r \Gamma_\beta G^a]$  is the transmission coefficient which depends on Coulomb potential through Green's function (see Eq.(2)). We emphasize here that the expression Eq.(24) satisfies gauge invariant condition, i.e., the heat current remains the same if the voltage of each terminal is shifted by a constant amount, as discussed in details in Ref.56. It is easy to see that the total heat current is nonzero,

$$\sum_\alpha I_\alpha^h = \sum_\alpha V_\alpha I_\alpha,$$

which is just the Joule heating. In particular, for a two-probe system,  $\sum_\alpha I_\alpha^h = (V_L - V_R)I_L$ .

Now, we can fix the voltage at each terminal  $V_\alpha = (V/2, -V/2, 0, 0)$  as before and expand the heat current in terms of voltage up to the second order, from which we have the following expression for the linear and second-order nonlinear heat conductance<sup>56</sup>

$$I_\alpha^h = I_\alpha^{h1} + I_\alpha^{h2},$$

where

$$I_\alpha^{h1} = -q \sum_\beta \int_E (E - E_F) (-\partial_E f) T_{\alpha\beta} V_\beta,$$



is the linear heat current and

$$I_\alpha^{h2} = q^2 \sum_{\beta\gamma} \int_E (E - E_F) (-\partial_E f) T_{\alpha\beta\gamma} V_\beta V_\gamma - (q^2/2) \sum_\beta \int_E (-\partial_E f) T_{\alpha\beta} (V_\alpha - V_\beta)^2, \quad (25)$$

is the second order nonlinear heat current, where  $T_{\alpha\beta\gamma}$  is defined by  $G_{\alpha\beta\gamma} \equiv \int_E (-\partial_E f) T_{\alpha\beta\gamma}$  through Eqs.(10),(11), and (12). When TR and inversion symmetries are preserved, it is easy to show that  $I_3^h - I_4^h = 0$  up to the second order in voltage, i.e., no transverse heat current. Similarly, the nonlinear transverse Hall current along the  $x$  direction is zero. It means that the nonzero transverse heat current is also a measure of the BCD-induced nonlinear Hall effect.

Now we consider the system with the mirror symmetry  $\mathcal{M}_x$ , i.e., Case 3. In this case, when the longitudinal bias voltage is applied, a longitudinal heat current is given by  $I_L^h = I_1^h - I_2^h$ . Moreover, accompanied with the generation of the Hall current, the transverse heat current occurs, which can be expressed as  $I_T^h = I_3^{h2} - I_4^{h2}$  because the first-order heat current in terminals 3 and 4 are zero. In addition, it is easy to show that the second term in Eq.(25) does not contribute to the transverse heat current due to the symmetry of linear conductance. Fig. 9 shows the longitudinal and transverse heat currents versus the Fermi energy  $E_F$  for different temperatures. In general, both longitudinal and transverse heat currents increase as the temperature increases and the longitudinal heat current is one order of magnitude larger than the transverse heat current. The transverse heat current in the first subband is negative while in the second and third subband is positive.

#### IV. CONCLUSION

To study the role of Berry curvature dipole in quantum transport, we have calculated the second-order nonlinear Hall resistance and Hall current, as well as the second-order nonlinear longitudinal and transverse heat current for a four-terminal system with time-reversal symmetry and mirror symmetry  $\mathcal{M}_x$ . Effects of the induced Coulomb interaction and the dephasing mechanism on nonlinear Hall response have also been investigated. It is found that the induced nonequilibrium Coulomb potential and the voltage profile of virtual probes have the same symmetry as that of the underlying system, which gives rise to two additional nonlinear Hall effects: (1) the nonlinear Hall effect due to induced nonequilibrium Coulomb potential and (2) the nonlinear Hall effect induced by dephasing. Moreover, the Berry curvature dipole can also be characterized by the transverse heat current in a four terminal setup that can be measured experimentally.

#### ACKNOWLEDGMENTS

This work was supported by the National Natural Science Foundation of China (Grant Nos. 12034014, 12174262, and

11774238), the Natural Science Foundation of Guangdong (Grant No. 2020A1515011418), and the Natural Science Foundation of Shenzhen (Grant Nos. 20200812092737002, JCYJ20190808150409413, and JCYJ20190808115415679).

#### V. APPENDIX

In this appendix, we derive symmetry relations in the third row of Table I using the boundary matching approach<sup>57,58</sup>. For Eq.(13), the basis wave function in free space is given by  $\Psi = (a, b)^T e^{ik_x x} e^{ik_y y}$  where  $T$  denotes the transpose and  $a$  and  $b$  depend on  $k_x$  and  $k_y$ . For a nanoribbon along the  $x$  direction with width  $L$ , the basis wave function becomes  $\Psi_n = \chi_n(y) e^{ik_n x}$  where  $\chi_n$  is a two-component wave function and the subband channel  $n$  is due to the boundary conditions  $\chi_n(0) = \chi_n(L) = 0$ . Similarly, for the nanoribbon along the  $y$  direction, we have the basis wave function  $\Psi_n = \bar{\chi}_n(x) e^{ik'_n y}$ .  $k_n$  and  $k'_n$  show that the velocities along  $x$  and  $y$  directions are different. For the four-terminal system, we divide the system into five regions: region I to region IV (terminal 1 to terminal 4) and region V (the central scattering region). The wave functions in regions I to IV can be expressed in a general form

$$\Psi_{rmI} = \sum_n \bar{\chi}_n(y) (a_n e^{-ik_n x} + b_n e^{ik_n x}), \quad (26)$$

$$\Psi_{rmII} = \sum_n \bar{\chi}_n(y) (c_n e^{-ik_n x} + d_n e^{ik_n x}), \quad (27)$$

$$\Psi_{rmIII} = \sum_n \chi_n(x) (e_n e^{-ik'_n y} + f_n e^{ik'_n y}), \quad (28)$$

$$\Psi_{rmIV} = \sum_n \chi_n(x) (g_n e^{-ik'_n y} + h_n e^{ik'_n y}). \quad (29)$$

And the wave function in region V is the combination of those in regions I, II, III, and IV,

$$\Psi_{rmV} = \sum_n \bar{\chi}_n(y) (u_n e^{-ik_n x} + v_n e^{ik_n x}) + \sum_n \chi_n(x) (w_n e^{-ik'_n y} + x_n e^{ik'_n y}).$$

From Eqs. (26)-(29), we see that coefficients  $b_n$ ,  $c_n$ ,  $e_n$ , and  $h_n$  correspond to the incident waves while coefficients  $a_n$ ,  $d_n$ ,  $f_n$ , and  $g_n$  correspond to the outgoing waves, from which the transmission and reflection coefficients can be obtained. To find the solution, we note that there are four interfaces at  $x = 0, L$  and  $y = 0, L$  when the origin is fixed at the lower-left corner of region V. By matching wave functions at the interfaces, we have  $\Psi_A = \Psi_B$  and  $\Psi'_A = \Psi'_B$  which gives 8 equations for four interfaces. For the electron in the first subband incident from terminal 1, we have  $b_n = \delta_{1n}$ ,  $c_n = e_n = h_n = 0$  (no electron coming from terminals 2, 3, and 4) leaving 8 unknown variables  $a_n$ ,  $d_n$ ,  $f_n$ ,  $g_n$ ,  $u_n$ ,  $v_n$ ,  $w_n$ , and  $x_n$ . Therefore the transmission coefficients  $T_{12} = \sum_n |d_n|^2 k_n / k_1$ ,  $T_{13} = \sum_n |f_n|^2 k'_n / k_1$ , and  $T_{14} = \sum_n |g_n|^2 k'_n / k_1$  as well as the reflection coefficient  $R_{11} = \sum_n |a_n|^2 k'_n / k_1$  can be solved<sup>57,58</sup>, where  $n$  goes from

1 to  $N$ . Note that due to the evanescent modes,  $N$  has to be large enough to guarantee the convergence. Transmission coefficients  $T_{31}, T_{32}, T_{34}$  and the reflection coefficient  $R_{33}$  can be obtained by assuming  $e_n = \delta_{1n}, b_n = c_n = h_n = 0$  and solving for other coefficients  $a_n, d_n, \dots$

Note that the mirror symmetry  $\mathcal{M}_y$  is broken in the Hamiltonian Eq.(13), but the potential  $V(x, y) = 0$  has the  $C_4$  symmetry. Therefore, if we change  $y$  to  $-y$ , we have  $\Psi_{rmIII}(y) = \Psi_{rmIV}(-y)$ . From Eqs.(28) and (29), we

have  $|f_n|^2 = |g_n|^2$ , from which we obtain  $T_{13} = T_{14}$  or  $G_{13} = G_{14}$ . To show  $R_{11} = R_{22}$  or  $G_{11} = G_{22}$ , we use the symmetry  $V(x, y) = V(-x, y)$ . Instead of  $b_n = \delta_{1n}, c_n = e_n = h_n = 0$  for  $R_{11}$ , we assume  $b_n = 0, c_n = \delta_{1n}$  and  $e_n = h_n = 0$  for  $R_{22}$ . From Eqs.(26) and (27), we see that the equations are symmetric if we change  $x$  to  $-x$ , hence we conclude  $G_{11} = G_{22}$ . Using similar argument, we can prove that  $G_{33} = G_{44}$ . However, since  $k_n \neq k'_n$ , we have  $G_{12} \neq G_{34}$  and  $G_{11} \neq G_{33}$ .

\* xufuming@szu.edu.cn

† jianwang@hku.hk

<sup>1</sup> I. Sodemann and L. Fu, Phys. Rev. Lett. **115**, 216806 (2015).

<sup>2</sup> T. Low, Y. Jiang, and F. Guinea, Phys. Rev. B **92**, 235447 (2015).

<sup>3</sup> Z. Z. Du, Hai-Zhou Lu, and X. C. Xie, Nat. Rev. Phys. (2021), <https://doi.org/10.1038/S42254-021-00359-6>.

<sup>4</sup> J. I. Facio, D. Efremov, K. Koepernik, J.-S. You, I. Sodemann, and J. van den Brink, Phys. Rev. Lett. **121**, 246403 (2018).

<sup>5</sup> Y. Zhang, Y. Sun, and B. Yan, Phys. Rev. B **97**, 041101(R) (2018).

<sup>6</sup> Z. Z. Du, C. M. Wang, H.-Z. Lu, and X. C. Xie, Phys. Rev. Lett. **121**, 266601 (2018).

<sup>7</sup> J.-S. You, S. Fang, S.-Y. Xu, E. Kaxiras, and T. Low, Phys. Rev. B **98**, 121109(R) (2018).

<sup>8</sup> Q. Ma, S.-Y. Xu, H. Shen, D. MacNeill, V. Fatemi, T.-R. Chang, A. M. Mier Valdivia, S. Wu, Z. Du, C.-H. Hsu, S. Fang, Q. D. Gibson, K. Watanabe, T. Taniguchi, R. J. Cava, E. Kaxiras, H.-Z. Lu, H. Lin, L. Fu, N. Gedik, and P. Jarillo-Herrero, Nature **565**, 337 (2019).

<sup>9</sup> S.-Y. Xu, Q. Ma, H. Shen, V. Fatemi, S. Wu, T.-R. Chang, G. Chang, A. M. M. Valdivia, C.-K. Chan, Q. D. Gibson, J. Zhou, Z. Liu, K. Watanabe, T. Taniguchi, H. Lin, R. J. Cava, L. Fu, N. Gedik, and P. Jarillo-Herrero, Nat. Phys. **14**, 900 (2018).

<sup>10</sup> K. Kang, T. Li, E. Sohn, J. Shan, and K. F. Mak, Nat. Mat. **18**, 324 (2019).

<sup>11</sup> J. Xiao, Y. Wang, H. Wang, C. D. Pemmaraju, S. Wang, P. Muscher, E. J. Sie, C. M. Nyby, T. P. Devereaux, X. Qian, X. Zhang, and A. M. Lindenberg, Nat. Phys. **16**, 1028 (2020).

<sup>12</sup> D. Kumar, C.-H. Hsu, R. Sharma, T.-R. Chang, P. Yu, J. Wang, G. Eda, G. Liang, and H. Yang, Nat. Nanotechnol. **16**, 421 (2021).

<sup>13</sup> T. H. Hsieh, H. Lin, J. Liu, W. Duan, A. Bansil, and L. Fu, Nat. Commun. **3**, 982 (2012).

<sup>14</sup> A. Lau and C. Ortix, Phys. Rev. Lett. **122**, 186801 (2019).

<sup>15</sup> R.-C. Xiao, D.-F. Shao, Z.-Q. Zhang, and H. Jiang, Phys. Rev. Appl. **13**, 044014 (2020).

<sup>16</sup> R.-C. Xiao, D.-F. Shao, W. Huang, and H. Jiang, Phys. Rev. B **102**, 024109 (2020).

<sup>17</sup> B. T. Zhou, C.-P. Zhang, and K. T. Law, Phys. Rev. Appl. **13**, 024053 (2020).

<sup>18</sup> R. Battilomo, N. Scopigno, and C. Ortix, Phys. Rev. Lett. **123**, 196403 (2019).

<sup>19</sup> S. S. Samal, S. Nandy, and K. Saha, Phys. Rev. B **103**, L201202 (2021).

<sup>20</sup> Y. Gao, F. Zhang, and W. Zhang, Phys. Rev. B **102**, 245116 (2020).

<sup>21</sup> R.-H. Li, O. G. Heinonen, A. A. Burkov, and Steven S.-L. Zhang, Phys. Rev. B **103**, 045105 (2021).

<sup>22</sup> C. Zeng, S. Nandy, and S. Tewari, Phys. Rev. B **103**, 245119 (2021).

<sup>23</sup> R. Battilomo, N. Scopigno, and C. Ortix, Phys. Rev. Res. **3**, L012006 (2021).

<sup>24</sup> P. A. Pantaleón, T. Low, and F. Guinea, Phys. Rev. B **103**, 205403 (2021).

<sup>25</sup> X.-Q. Yu, Z.-G. Zhu, J.-S. You, T. Low, and G. Su, Phys. Rev. B **99**, 201410(R) (2019).

<sup>26</sup> C. Zeng, S. Nandy, and S. Tewari, Phys. Rev. Research **2**, 032066(R) (2020).

<sup>27</sup> C. Texier and M. Büttiker, Phys. Rev. B **62**, 7454 (2000).

<sup>28</sup> S. Oberholzer, E. Bieri, C. Schönenberger, M. Giovannini, and J. Faist, Phys. Rev. Lett. **96**, 046804 (2006).

<sup>29</sup> Z. Z. Du, C. M. Wang, S. Li, H. -Z. Lu, and X.C. Xie, Nat. Commun. **10**, 3047 (2019).

<sup>30</sup> Z. Z. Du, C. M. Wang, H. -P. Sun, H. -Z. Lu, and X.C. Xie, Nat. Commun. **12**, 5038 (2021).

<sup>31</sup> M. Büttiker, J. Phys.: Condens. Matter **5**, 9361 (1993).

<sup>32</sup> M. Büttiker and T. Christen, in *Quantum Transport in Semiconductor Submicron Structures*, edited by B. Kramer, (Kluwer Academic Publishers, Dordrecht, 1996, pp263).

<sup>33</sup> M. Büttiker, Phys. Rev. B **33**, 3020 (1986).

<sup>34</sup> Y. Xing, Q.-f. Sun, and J.Wang, Phys. Rev. B **77**, 115346 (2008).

<sup>35</sup> H. Jiang, S. Cheng, Q.-f. Sun, and X. C. Xie, Phys. Rev. Lett. **103**, 036803 (2009).

<sup>36</sup> M. Moskalets and M. Büttiker, Phys. Rev. B **64**, 201305(R) (2001).

<sup>37</sup> R. Golizadeh-Mojarad and S. Datta, Phys. Rev. B **75**, 081301(R) (2007).

<sup>38</sup> Y. Blanter and M. Büttiker, Phys. Rep. **336**, 1 (2000).

<sup>39</sup> Z. S. Ma, J. Wang and H. Guo, Phys. Rev. B **57**, 9108 (1998).

<sup>40</sup> B. Wang, J. Wang, and H. Guo, J. Appl. Phys. **86**, 5094 (1999).

<sup>41</sup> L. Zhang, B. Wang, and J. Wang, Phys. Rev. B **86**, 165431 (2012).

<sup>42</sup> The injectivity was first introduced by M. Büttiker in the context of scattering matrix theory and then be expressed with the Green's function<sup>43</sup>.

<sup>43</sup> T. Gramschpacher and M. Büttiker, Phys. Rev. B **56**, 13026 (1997).

<sup>44</sup> Z. S. Ma, J. Wang and H. Guo, Phys. Rev. B **59**, 7575 (1999).

<sup>45</sup> I.B. Levinson, Sov. Phys. JETP **68**, 1257 (1989); Zh. Eksp. Teor. Fiz. **95**, 2175 (1989).

<sup>46</sup> For simplicity, we have neglected terms such as  $\partial_E \Sigma^r(E)$ .

<sup>47</sup> T. Christen and M. Büttiker, Europhys. Lett. **35**, 523 (1996).

<sup>48</sup> M. K. Yip, J. Wang and H. Guo, Z. Phys. B: Condens. Matter **104**, 463 (1997).

<sup>49</sup> W. D. Sheng, J. Wang, and H. Guo, J. Phys.: Condens. Matter **10**, 5335 (1998); W. D. Sheng, Q. Zheng, J. Wang, and H. Guo, Phys. Rev. B **59**, 538 (1999).

<sup>50</sup> M. Papaj and L. Fu, Phys. Rev. Lett. **123**, 216802 (2019).

<sup>51</sup> Y. Tanaka, Z. Ren, T. Sato, K. Nakayama, S. Souma, T. Takahashi, K. Segawa, and Y. Ando, Nature Physics **8**, 800 (2012).

<sup>52</sup> Y. Xing, Q.F. Sun, and J. Wang, Phys. Rev. B **80**, 235411 (2009).

<sup>53</sup> M. Wei, M. Zhou, B. Wang, and Y. Xing, Phys. Rev. B **102**, 075432 (2020).

<sup>54</sup> D. Xiao, M.-C. Chang, and Q. Niu, Rev. Mod. Phys. **82**, 1959

- (2010).
- <sup>55</sup> Y. J. Wang, J. Wang, and H. Guo, Phys. Rev. B **47**, 4348 (1993).
- <sup>56</sup> J. Chen, M. ShangGuan, and J. Wang, New J. Phys. **17** 053034 (2015).
- <sup>57</sup> R. L. Schult, D. G. Ravenhall, and H. W. Wyld, Phys. Rev. B **39**, 5476 (1989).
- <sup>58</sup> J. Wang, Y. J. Wang, and H. Guo, Phys. Rev. B **46**, 2420 (1992).